Mat. Res. Soc. Symp. Proc. Vol. 674 © 2001 Materials Research Society

Nanocrystalline and Nanostructured High-Performance Permanent Magnets

D. Goll, W. Sigle, G.C. Hadjipanayis[1] and H. Kronmüller
Max-Planck-Institut für Metallforschung, Heisenbergstr. 1, D-70569 Stuttgart, Germany
[1] University of Delaware, Newark, U.S.A.

ABSTRACT

The rather complex correlation between the microstructure and the magnetic properties is demonstrated for two types of high-quality RE-TM permanent magnets (pms), namely nanocrystalline $RE_2Fe_{14}B$ (RE = Nd,Pr) and nanostructured $Sm_2(Co,Cu,Fe,Zr)_{17}$ pms. The detailed analysis of this correlation for both pm materials leads to a quantitative comprehension of the hardening mechanism enabling the optimization of their magnetic properties and temperature dependences. In the case of $RE_2Fe_{14}B$, isotropic bonded pms are fabricated showing maximum energy products in the order of 90 kJ/m^3. In the case of $Sm_2(Co,Cu,Fe,Zr)_{17}$, magnets with excellent high-temperature magnetic properties are tailored. Hereby, the investigations in addition provide important clues to the evolution of the characteristic microstructural and magnetic properties and to the role of the involved elements.

INTRODUCTION

Modern high-quality permanent magnets (pms) are based on RE-TM intermetallic compounds of rare earth (RE = Nd,Pr,Sm) and transition metals (TM = Fe,Co) [1–4]. With these compounds outstanding intrinsic magnetic properties, large magnetocrystalline anisotropy constants $K_1 > 10^6$ J/m^3, large spontaneous polarizations $J_S > 1.2$ T and Curie temperatures $T_C > 250$°C as well as optimized microstructures can be realized. A large spontaneous polarization is a prerequisite for high remanences J_R, whereas a large magnetocrystalline anisotropy constant may result in large coercivities both ensuring high maximum energy products $(BH)_{max} \leq J_R^2/(4\mu_0)$ ($\mu_0 = 4\pi \cdot 10^{-7}$ Vs/Am) as long as the condition $\mu_0 H_C > 0.5 J_R$ holds. The ternary systems $RE_2Fe_{14}B$ (RE = Nd,Pr) [5] are currently considered to be the highest performance pm materials at all because of their very large spontaneous polarization of 1.6 T resulting in maximum energy products $(BH)_{max}$ up to 15 times larger than for ferrites. The only disadvantage of such magnets are their comparatively low Curie temperatures of $T_C \approx 300$°C. Nevertheless, nanocrystalline magnetic materials of this system have opened a new class of pm materials which are optimally suitable for high-performance polymer bonded magnets. Pms which supply the highest $(BH)_{max}$ values at elevated temperatures (beyond which $RE_2Fe_{14}B$ is no longer viable) are based on the quintary system $Sm_2(Co,Cu,Fe,Zr)_{17}$ [5]. With such magnets coercivities as large as 1 T can be realized even at 500°C which makes them suitable for high temperatures [6,7].

For a further improvement of the performance of polymer bonded magnets and the high-temperature magnetic properties, especially the temperature stability of the coercivity, the most important prerequisite for both hard magnetic materials is the detailed analysis of the hardening mechanisms and in the case of $Sm_2(Co,Cu,Fe,Zr)_{17}$ additionally of its formation. It is nowadays generally accepted that in $RE_2Fe_{14}B$ based materials the nucleation mechanism governs the coercivity, whereas in Sm_2Co_{17} based materials domain wall pinning processes are dominant. For both hardening mechanisms the coercivity is well-described by the following global formula [8]:

$$\mu_0 H_C = \mu_0 \alpha \frac{2K_1}{J_S} - N_{eff} J_S \qquad (1)$$

with the microstructural parameters α and N_{eff} describing the effect of the real microstructure, i.e. all deviations from the ideal crystal structure. Some recent results concerning the interpretation of hardening mechanisms in nanocrystalline or nanostructured pms will be discussed in the following sections.

EXPERIMENTAL

There are two principial processing routes for manufacturing high-quality pms – sintering and melt-spinning leading to microcrystalline (anisotropic) and nanocrystalline (isotropic) microstructures, respectively. Our studies were performed on nanocrystalline exchange coupled $Pr_2Fe_{14}B$ type melt-spun ribbons and polymer bonded specimens made out of them as well as on sintered and melt-spun $Sm_2(Co,Cu,Fe,Zr)_{17}$ type pms. For the melt-spun ribbons master alloys of different nominal compositions have been prepared by arc melting from the constituent elements and a FeB prealloy in the case of PrFeB. By using the melt-spinning technique the ingots were directly quenched into nanocrystalline ribbon flakes whereby in all cases the processing conditions were optimized. For the polymer bonded magnets the melt-spun ribbons were crushed into powder (powder particle size: $1-40\,\mu$m) and then industrially fabricated into isotropic bonded magnets (density 6.0 g/cm^3) by mixing the powder with a polymer (4.5wt% epoxy resin, 0.5wt% Zn-stearat) followed by compression molding the resulting compound at a pressure of 7 t/cm^2 without a magnetic field. For the sintered samples a commercial solution heat treated sintered magnet of the nominal composition $Sm(Co_{bal}Cu_{0.07}Fe_{0.22}Zr_{0.04})_{7.4}$ has been taken. For the annealing procedures the samples have been wrapped into Ta foils and sealed in quartz tubes with Ar.

For the microstructural investigations different types of electron microscopy have been used: 1. (High resolution) transmission electron microscopy HRTEM (Philips CM200) for imaging the morphology and crystal lattices of the microstructure. 2. Lorentz microscopy (Philips CM200) in the Fresnel and Foucault mode for visualizing the domain wall pattern. 3. High resolution energy dispersive X-ray analysis (EDX) in a dedicated scanning TEM (VG HB501) to determine the chemical compositions of the three phases involved. Due to the very high spatial resolution of 1 nm the latter technique can be also used to measure compositional changes between different phases. Here, it should be noticed, that such profiles are a convolution of the real chemical profile and the resolution function of the probe. The magnetic measurements were performed in a vibrating sample magnetometer (PAR VSM) with a maximum field of 9 T. The external field was corrected by the demagnetization field ($\mu_0 H = \mu_0 H_{ext} - NJ$) with the macroscopic demagnetization factor N of the order of 0.01 (ribbons) and 0.33 (bonded/bulk magnets), respectively. The magnetic field was applied parallel to the ribbon direction or to the texture axis.

NANOCRYSTALLINE MAGNETS

Nanocrystalline hard magnets on the basis of $RE_2Fe_{14}B$ are suitable for tailoring magnets with definite properties of the hysteresis loop. Based on the ternary phase diagram three types of nanocrystalline pms with different microstructures have been developed (see figure 1) – magnets with RE excess (decoupled magnets), stoichiometric magnets and magnets with overstoichiometric Fe (composite magnets) [9–16].

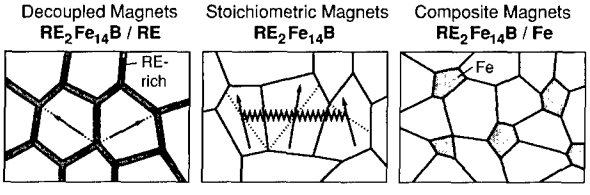

Figure 1. Schematic microstructures (remanent state) for the three different types of nanocrystalline $RE_2Fe_{14}B$ based magnets (RE = Nd,Pr).

Exchange coupled magnets

Whereas in decoupled magnets the hard magnetic grains are isolated by a RE-rich paramagnetic intergranular layer limiting the remanence to rather low values, i.e. $J_R \leq 0.5\,J_S$, the rema-

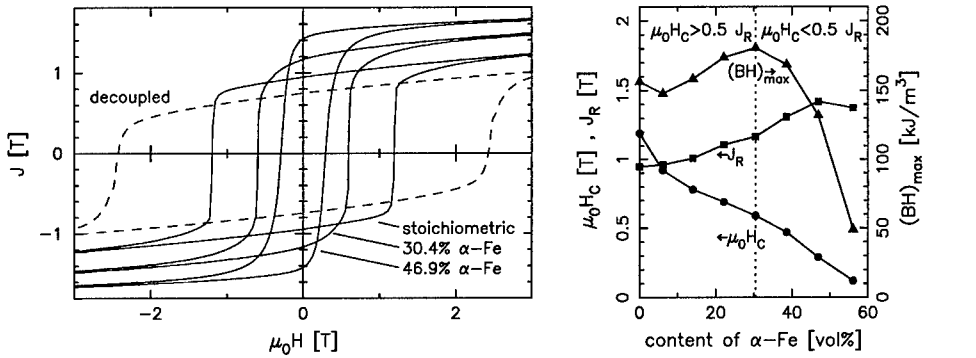

Figure 2. Room temperature hysteresis loops of PrFeB based pms: $Pr_{15}Fe_{78}B_7$ (decoupled grains), $Pr_{12}Fe_{82}B_6$ (stoichiometric, exchange coupled grains), $Pr_8Fe_{87}B_5$ (30.4% α-Fe) and $Pr_6Fe_{90}B_4$ (46.9% α-Fe) (composite, exchange coupled grains) (*left*). Magnetic properties of composite PrFeB pms measured at room temperature as a function of excess α-Fe (*right*).

nence and therefore $(BH)_{max}$ are significantly increased in exchange coupled magnets (stoichiometric and composite) due to the effect of exchange coupling between the grains. In stoichiometric magnets the hard magnetic grains are directly connected and therefore magnetically coupled by exchange interactions, i.e. the polarization direction underlies a smooth transition from the easy axis of one hard magnetic grain to the easy axis of another one on the scale of the so-called Bloch wall width $\delta_B = \pi(A/K_1)^{0.5} = \pi l_K$ (A: exchange constant, l_K: exchange length) which is in the order of 4 nm for $RE_2Fe_{14}B$. Or, in other words, within the wall width δ_B a magnetic texture is induced with the texture axis parallel to the original saturation polarization (i.e. the direction of the initially applied field). Since only this exchange coupled volume fraction causes the remanence enhancement the grain size should be smaller than four times the exchange length l_K in order to notice an efficient remanence enhancing effect macroscopically [17]. In composite magnets beside the hard magnetic $RE_2Fe_{14}B$ grains nanocrystalline soft magnetic α-Fe grains occur as a consequence of the overstoichiometric α-Fe leading to a further significant increase of the remanence. In this case, remanence enhancing is due to exchange coupling among the grains and to the large spontaneous polarization of α-Fe ($J_S = 2.15$ T) which drastically intensifies the magnetic texturing effect. For a complete exchange hardening and therefore excellent hard magnetic properties it is imperative that the grain size of the soft magnetic grains is in the order of the Bloch wall width δ_B of the hard magnetic phase.

Figure 2 illustrates the enormous effect of exchange coupling by comparing the room temperature hysteresis loops of the different types of nanocrystalline PrFeB based magnets with each other. Additionally, figure 2 summarizes the changes of the room temperature magnetic properties with varying α-Fe content. For an iron excess of 30.4% the observed J_R is 1.17 T, i.e., an increase of 51% as compared to the isotropic value of 0.78 T and $(BH)_{max}$ amounts to 180.7 kJ/m^3. With increasing α-Fe concentration besides the remanence enhancement the coercivity decreases continuously. However, as long as the condition $\mu_0 H_C > 0.5 J_R$ is fulfilled, $(BH)_{max}$ increases. Otherwise, $(BH)_{max}$ is restricted by irreversible demagnetization processes. For stoichiometric $Pr_{12}Fe_{82}B_6$ the average grain size amounts to 20 nm whereas in the case of the $Pr_8Fe_{87}B_5$ composite magnet a mixture of hard magnetic $Pr_2Fe_{14}B$ grains (grain size 20 – 30 nm) and soft magnetic α-Fe grains (grain size $\approx$ 15 nm) is found [11].

Polymer bonded magnets

Exchange coupled grain structures are optimally suitable for the industrial fabrication of polymer bonded magnets because of their high $(BH)_{max}$ values and their low RE content compared to

conventional magnets which reduces the cost of the raw materials and improves the corrosion resistance. With bonded magnets which are characterized by low brittleness, low electric conductivity and their isotropy any desired shape can be prepared directly. In figure 3 the room temperature hysteresis loops of polymer bonded pms can be seen in comparison with the loops of the corresponding ribbon material using a stoichiometric and a composite alloy. It is obvious from this, that the rectangularity or squareness of the hysteresis loops is reduced for bonded magnets which may be due to the large number of ribbons used for powderizing with their magnetic properties varying slightly. Nevertheless, in both cases the coercive field corresponds approximately to that of the as melt-spun ribbons. Despite the reduction of the remanence for bonded pms due to the diluting effect of the polymer $(BH)_{\max}$ values up to 90 kJ/m^3 can be received.

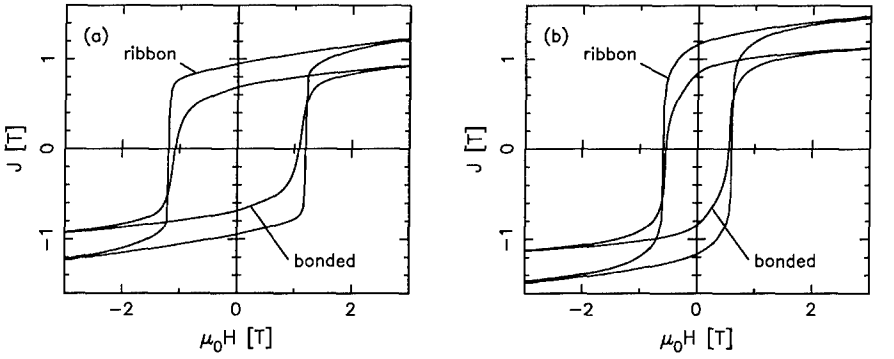

Figure 3. Room temperature hysteresis loops of polymer bonded powders compared to the corresponding ribbon material: (a) $Pr_2Fe_{14}B$ (stoichiometric pm) and (b) $Pr_2Fe_{14}B$/30.4vol% α-Fe (composite pm).

Coercivity mechanism

As shown in figure 4 (left), the temperature stability of the coercivity is better for the exchange coupled magnets (including polymer bonded magnets) than for the decoupled magnet. Using eq. (1) the temperature dependence of the coercivity can be analyzed quantitatively within the framework of the theory of micromagnetism. For nanocrystalline (nucleation hardened) magnets, the microstructural parameter α in general is composed of three subparameters ($\alpha = \alpha_K \alpha_{ex} \alpha_\psi$) [8, 18], namely α_K which describes the effect of the grain boundaries where the magnetocrystalline anisotropy is reduced ($\alpha_K \approx 0.8$) and α_{ex} taking into account the effect of the exchange coupling between neighbouring grains ($\alpha_{ex} = 1$ for decoupled magnets). The parameter α_ψ denotes the effect of misaligned grains and can be substituted in the case of isotropic magnets by the minimum nucleation field $H_N^{min} = \alpha_\psi 2K_1/J_S$, since the most unfavourably oriented grains (misorientation angle $\psi \approx 45°$) govern the whole demagnetization process. H_N^{min} is determined by the intrinsic material parameters J_S, K_1 and K_2 which are well-known from single crystals. If the nucleation model is valid, plotting the experimental data $\mu_0 H_C/J_S$ versus the theoretical values should yield a straight line with slope $\alpha_K \alpha_{ex}$ and ordinate intersection $(-N_{eff})$ in the case of temperature independent microstructural parameters. In figure 4 (right) the results of this evaluation are represented for the three different types of nanocrystalline PrFeB magnets and in addition for the bonded magnets made from stoichiometric and 30.4% excess iron ribbons, respectively. In fact, in all cases an approximately linear behaviour is observed, i.e., the dominant process for the magnetization reversal is the nucleation of reversed domains.

In general, the $\alpha_K \alpha_{ex}$ and N_{eff} values of the composite magnets are significantly smaller than for the decoupled magnet. The decrease of $\alpha_K \alpha_{ex}$ reflects the decrease in the coercivity and can

be attributed to the low anisotropy constant of α-Fe and to the exchange coupling between the grains inducing cooperative demagnetization processes of clusters of grains. On the other hand, the decrease in N_{eff} is caused by a more spherical grain shape and by a reduction of local stray fields at the edges and corners of the grains due to the smoothing effect of the exchange interaction at the grain boundaries. It is of interest to note that the microstructural parameters $\alpha_K \alpha_{ex}$ and N_{eff} for the bonded magnets are nearly the same as for their fully dense counterpart.

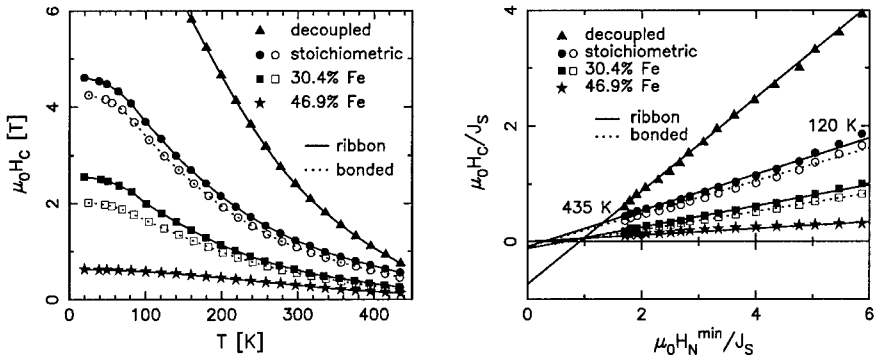

Figure 4. (*Left*) Temperature dependence of the coercivity. (*Right*) $\mu_0 H_C/J_S$ versus $\mu_0 H_N^{\text{min}}/J_S$ plot to determine the microstructural parameters for different nanocrystalline PrFeB pms. Decoupled: $\alpha_K \alpha_{ex} = 0.8$, $N_{\text{eff}} = 0.74$, stoichiometric: $\alpha_K \alpha_{ex} = 0.32$, $N_{\text{eff}} = 0.09$, stoichiometric/bonded: $\alpha_K \alpha_{ex} = 0.29$, $N_{\text{eff}} = 0.09$, composite (30.4% Fe): $\alpha_K \alpha_{ex} = 0.18$, $N_{\text{eff}} = 0.12$, composite (30.4% Fe)/bonded: $\alpha_K \alpha_{ex} = 0.16$, $N_{\text{eff}} = 0.12$, composite (46.9% Fe): $\alpha_K \alpha_{ex} = 0.06$, $N_{\text{eff}} = 0.00$.

NANOSTRUCTURED PERMANENT MAGNETS

$Sm_2(Co,Cu,Fe,Zr)_{17}$ magnets owe their outstanding magnetic properties exclusively to their complicated nanostructure (figure 5) consisting of three different phases: 1. Fe-rich pyramidal cells of the rhombohedral (R) 2:17 structure. 2. Cu-rich cell boundaries of the hexagonal (H) 1:5 structure. 3. Zr-rich lamellar platelets of the hexagonal 2:17 structure. The nanostructure develops in a self-organized process inside the μm-scaled grains during a complex three-step annealing

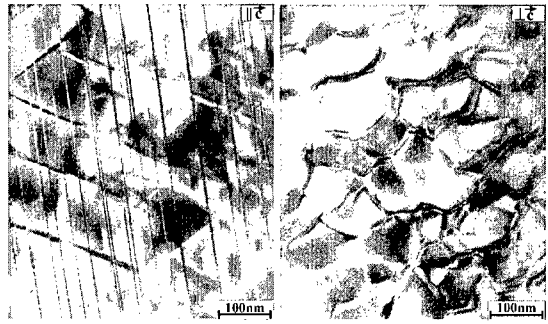

Figure 5. TEM micrographs of the nanostructure of a $Sm_2(Co,Cu,Fe,Zr)_{17}$ based sintered magnet. (*Left*) Rhombic structure observed parallel to the c-axis. (*Right*) Hexagonal network observed perpendicular to the c-axis.

procedure composed of homogenization, isothermal aging and slow cooling and causes a pinning type hardening mechanism, i.e., repulsive (or attractive) pinning of domain walls at (in) the 1:5 cell walls.

Evolution mechanism

It is generally agreed, that homogenization is required to obtain a single-phase 1:7 precursor alloy, i.e. a partly disordered R2:17 structure. This first step of the annealing procedure has been performed commercially at about 1200°C and will not be subject of the paper. During isothermal aging at 800°C the morphology of the nanostructure develops completely. As illustrated in figure 6 (left), this second step of the heat treatment is characterized by a continuous increase of the cell size and the lamellae density up to 110 nm and 0.043/nm after aging for 16 h, respectively, whereas the subsequent slow cooling procedure down to 400°C (cooling rate 1°C/min) followed by quenching to room temperature does not affect the morphology any more. It should be mentioned that the higher the aging temperature T_a is chosen, the larger the cell size is, however, the density of the lamellae increases only slightly. Our systematic study could solve the long lasting debate concerning the exact sequence of transformations by means of which the precursor alloy separates into the three phases present in the microstructure of the aged alloy. As proposed by Maury et al. [19] the ordering of the R2:17 phase induces the formation of the cell boundary phase whereas the platelet phase is generated less rapidly leading to a further ordering of the R2:17 phase. Hence, the results of Ray and Liu [20] according to which the lamellar Z-phase is created before the cell boundary phase could not be confirmed.

One of the most striking phenomena of the 2:17 based pms is the fact that after the isothermal aging the coercive field is only of the order of 0.1 T although the morphology of the three phases is fully developed. For receiving significant coercivity values slow cooling to lower temperatures (< 650°C) is absolutely necessary. In figure 6 (right) the annealing procedure is correlated with the coercive field and the (effective) magnetocrystalline anisotropy constant measured at room temperature. As will be shown in the following, the development of the typical hard magnetic properties has both chemical and structural reasons. The microchemical changes determined by using EDX which occur during aging are summarized in figure 7 for the matrix phase, the cell boundary phase and the lamellar Z-phase. It is obvious from this, that the lamellae are formed during the isothermal annealing at 800°C where they even develop their final chemical composition. Consequently, the evolution of the typical hard magnetic properties cannot be attributed to the lamellae as Katter [21] mistakenly presumed. In contrary, the chemical composition of the 1:5 cell boundary phase is mainly developed during the cooling procedure. Actually, during isothermal aging there is only a

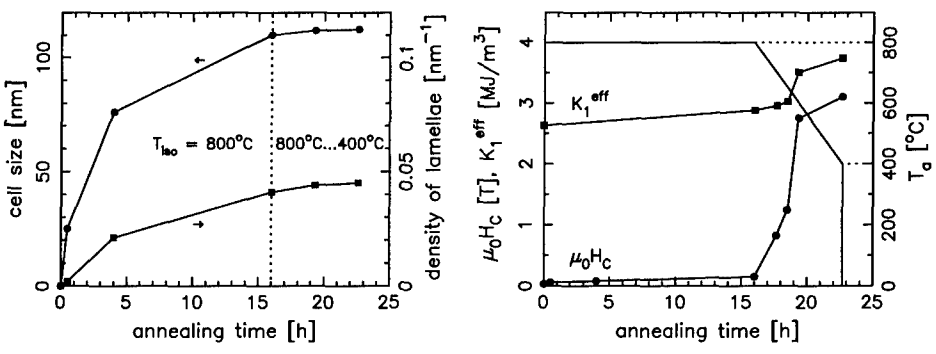

Figure 6. Evolution of the microstructural and hard magnetic properties for a sintered $Sm(Co_{bal}Cu_{0.07}Fe_{0.22}Zr_{0.04})_{7.4}$ pm during the aging program: (*Left*) Morphology of the microstructure. (*Right*) Coercivity $\mu_0 H_C$ and (effective) magnetocrystalline anisotropy constant K_1^{eff}.

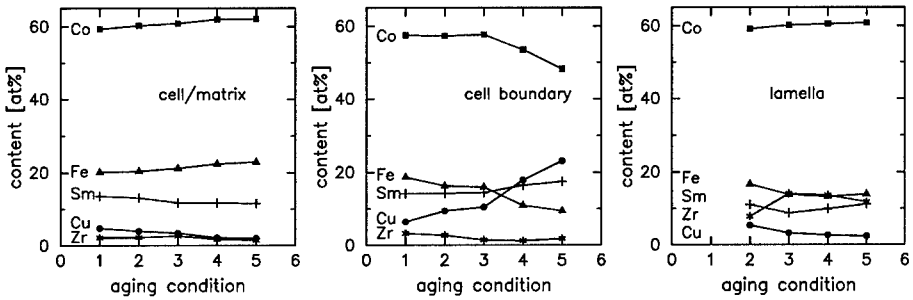

Figure 7. Chemical compositions (absolute accuracy $\pm(0.5-1.5)$ at%) of the cells, cell boundaries and lamellae determined by EDX for the $Sm(Co_{bal}Cu_{0.07}Fe_{0.22}Zr_{0.04})_{7.4}$ sintered magnet in different stages of the complex heat treatment: 1: T_a = 800 °C / t_a = 0.5 h, 2: T_a = 800 °C / t_a = 4 h, 3: T_a = 800 °C / t_a = 16 h, 4: same as 3 but cooled to 600 °C and 5: final state.

weak tendency for an enrichment of Cu or a depletion of Fe found, while during cooling the amount of Cu (Fe) increases (decreases) substantially in this phase by a factor of 3 (2) compared to state 1. Simultaneously, the Cu content decreases within the cells, whereas the Fe content increases. In addition, the development of the elemental profiles within the cell and the cell wall is characterized by a sharpening of the transition region between the 2:17 and the 1:5 phase as can be seen for Cu from figure 8 (left) for the different aging conditions. The distribution of all five elements after the slow cooling procedure down to 400°C is represented in figure 8 (right). Hereby, it is noteworthy, that Zr, Co and Fe are diluted within the cell walls. From a structural point of view, the slow cooling is also necessary for the development of the hexagonal 1:5 crystal structure of the cell walls. Although almost from the beginning of the isothermal aging, i.e. as soon as a cellular-like structure becomes visible, a 1:5 stoichiometry is obtained for the cell boundary phase, its crystal structure is not formed during isothermal aging. This is supported by X-ray diffraction spectra received before and after the cooling procedure. In order to detect [0 0 n] reflexes of high intensity in the diffraction spectra the samples were prepared perpendicular to the c-axis. According to figure 9 and table I after the isothermal heat treatment the following phases could be identified: rhombohedral and hexagonal Sm_2Co_{17}, rhombohedral Sm_2Co_7 and hexagonal Sm_5Co_{19}. However, the $SmCo_5$ phase is not present in this state. After cooling down to 400°C the Sm_2Co_7 and Sm_5Co_{19} phases have nearly vanished, but in addition besides the Sm_2Co_{17} phases (cells and lamellae) the $SmCo_5$ phase

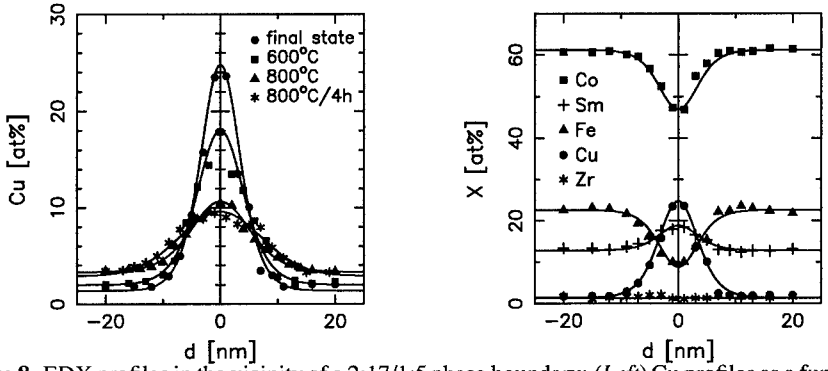

Figure 8. EDX profiles in the vicinity of a 2:17/1:5 phase boundary: (*Left*) Cu profiles as a function of the annealing program. (*Right*) Profiles of the elements Sm, Co, Cu, Fe and Zr for the final state.

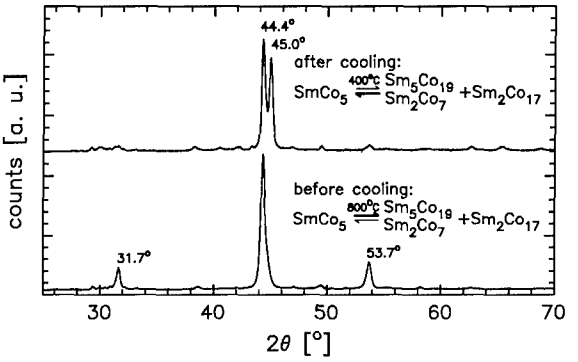

Figure 9. X-ray diffraction spectrum (CuK_α-radiation, $\lambda = 1.5406$ Å) of the $Sm(Co_{bal}Cu_{0.07}Fe_{0.22}Zr_{0.04})_{7.4}$ sintered pm prepared perpendicular to the c-axis (before and after the slow cooling procedure).

Phase	[h k l]	d^{theo} [Å]	d^{exp} [Å]	$2\theta^{exp}$ [°]
$SmCo_5$	[0 0 2]	1.989	2.013	45.0
$SmCo_{3.3}Cu_{1.7}$	[0 0 2]	2.012	2.013	45.0
Sm_2Co_{17} (R)	[0 0 6]	2.029	2.039	44.4
Sm_2Co_{17} (H)	[0 0 4]	2.041	2.039	44.4
Sm_2Co_7 (R)	[0 0 13]	2.806	2.820	31.7
Sm_5Co_{19} (H)	[0 0 19]	1.698	1.705	53.7

Table I. The lattice parameters d^{exp} determined from the diffraction peaks ($2\theta^{exp}$) marked in figure 9 in comparison with the reference data d_{theo} [22,23].

(cell walls) now appears. This behaviour reflects the eutectoid decomposition reaction of binary $SmCo_5$ into Sm_5Co_{19}, Sm_2Co_7 and Sm_2Co_{17} at 800°C [24] and the substantial decrease of this decomposition temperature to lower temperatures if some of the Co in $SmCo_5$ is substituted by Cu [25]. Consequently, according to these results the development of the typical hard magnetic properties during the cooling procedure is a complex process where by the diffusion of Cu into the cell walls and the decreasing temperature the thermodynamic phase equilibrium is shifted to the 1:5 phase.

Coercivity mechanism

According to the above results, it is the cell wall and not the lamellar Z-phase which is directly involved in the coercivity mechanism. Using Lorentz microscopy, the magnetic domain wall pattern (md) can be visualized (figure 10). These studies cleary show the zig-zag pinning of the domain walls (dw) along the elongated 1:5 cell boundaries, which is not affected by the lamellae present. Nevertheless, the lamellae are the most important prerequisite for a good stability of the precipitation structure. Indeed, according to high-resolution TEM studies the transition between the different phases is comparatively sharp and a large coherency of the various crystal lattices is observed despite their different lattice parameters (figure 11 (left)). Obviously, the occuring internal stresses are reduced by the lamellar Z-phase. This is suggested also by the fact that in Zr-free samples the lamellar phase does not exist and only Cu-rich ellipsoidal precipitations are found (figure 11 (right)), resulting in rather low coercivities. The pinning type hardening mechanism becomes also evident from the values for the microstructural parameters $\alpha_{K,pin}$ and $\alpha_{\psi,pin}$ obtained from $\mu_0 H_C/J_S$ versus $2\mu_0 K_1/J_S^2$ plots according to eq. (1) and from the dependence of

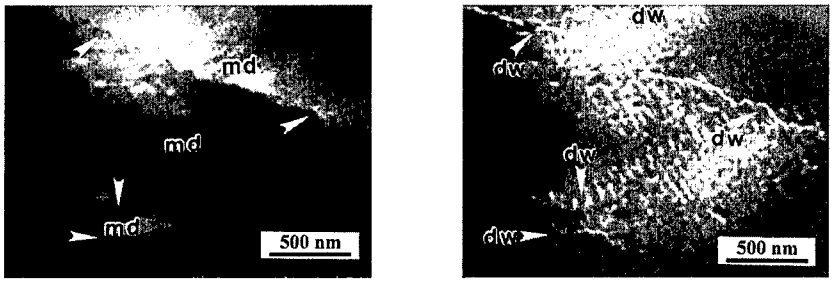

Figure 10. Lorentz microscopy images of a fully heat treated $Sm(Co_{bal}Cu_{0.07}Fe_{0.22}Zr_{0.04})_{7.4}$ sintered magnet: Foucault mode (left), Fresnel mode (right).

the coercivity of the misalignment angle ψ using Kerr microscopy, respectively. In fact, the parameter $\alpha_{K,pin}$ which is a measure for the strength of the domain wall pinning centers amounts to $0.1-0.4$ for fully heat treated samples depending on the aging conditions (figure 12 (left)) and for the parameter $\alpha_{\psi,pin}$ the typical $1/\cos\psi$ behaviour with increasing ψ is found, i.e. $\alpha_{\psi,pin} \geq 1$ (figure 12 (right)).

From the elemental profiles of figure 8 (right) the compositions of the pure phases are known. Hence, for the pure phases the intrinsic magnetic properties can be determined [26,27]. When these results are correlated as can be seen in figure 13 the schematic crystal energy profile proposed by Kronmüller [28] could be confirmed quantitatively. Accordingly, in the present case the cell walls act as repulsive barriers for domain walls since their domain wall energy is much larger than that of the 2:17 cells ($\gamma^{1:5} = 0.032\,\mathrm{J/m^2}$, $\gamma^{2:17} = 0.020\,\mathrm{J/m^2}$). The coercivity of 2:17 based pms can be analyzed quantitatively on the basis of micromagnetic models. Hereby, one takes advantage of theories which has been developed by several authors in terms of the continuum model [29] and of the Heisenberg model [30] to describe the pinning behaviour of domain walls by planar defects. According to that, a first approximation of the coercive field may be obtained from the maximum change in the domain wall energy with position. Supposing a linear increase of the wall energy over the range r_0 the coercivity may be written as

$$\mu_0 H_c = \mu_0 \frac{1}{2J_s} \left.\frac{\mathrm{d}\gamma}{\mathrm{d}z}\right|_{max} = \mu_0 \frac{1}{2J_s} \frac{|\gamma^{1:5} - \gamma^{2:17}|}{r_0} \,. \tag{2}$$

Within the range $r_0 \approx 2\,\mathrm{nm}$ the intrinsic material parameters vary between the cells and the cell boundaries. The sample under consideration yields a coercivity of $\mu_0 H_c = 2.7\,\mathrm{T}$ at room tem-

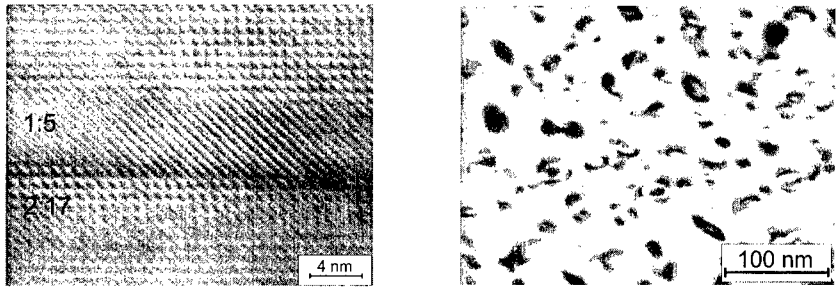

Figure 11. (*Left*) High-resolution TEM micrograph of the phase boundary between the cell (2:17) and the cell wall (1:5). (*Right*) Microstructure of a fully heat treated Zr-free $Sm(Co_{bal}Cu_{0.08}Fe_{0.1})_{8.5}$ alloy.

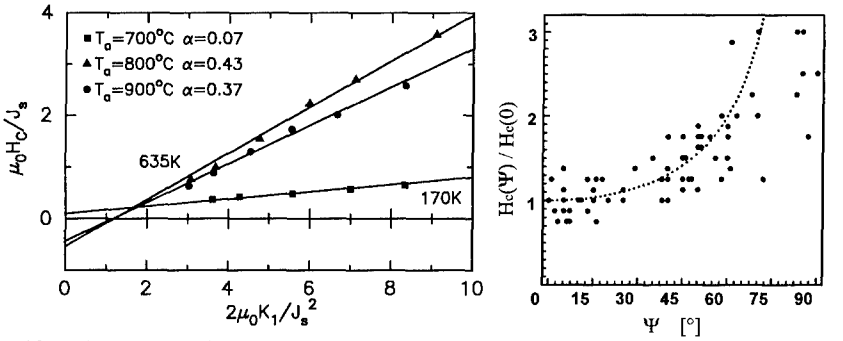

Figure 12. Microstructural parameters of a fully heat treated $Sm(Co_{bal}Cu_{0.07}Fe_{0.22}Zr_{0.04})_{7.4}$ sintered pm. (*Left*) Pinning strength $\alpha = \alpha_{K,pin}$ as function of the aging temperature T_a. (*Right*) $\alpha_{\psi,pin}$.

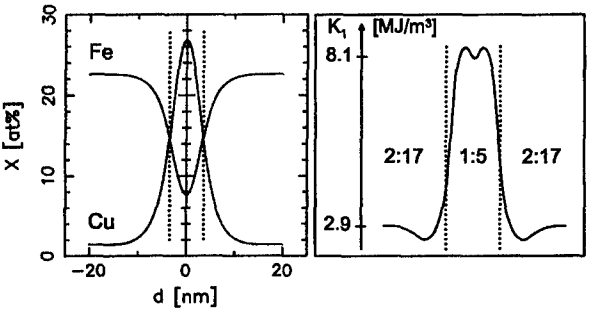

Figure 13. Calculated profile of the magnetocrystalline anisotropy constant K_1 in the vicinity of a 2:17/1:5 phase boundary using the results of the (deconvoluted) EDX Cu-profile.

perature and of 1.1 T at 200°C agreeing rather well with the measured temperature dependence of the coercivity. In a second approximation which is closely related to the first one the transition region between the 2:17 and the 1:5 phase is described by n individual lattice planes of distance $d = 0.2$ nm. Each plane i is characterized by a local anisotropy constant K_1^i and an exchange constant $A^{i,i+1}$ between neighbouring planes. Minimizing the total energy of this planar configuration results in:

$$\mu_0 H_C = \mu_0 \frac{\pi}{3\sqrt{3}} \frac{2K_1}{J_S} \frac{1}{\cos\psi_0} \frac{d}{\delta_B} \left| \sum_{i=1}^{n-1} \frac{A}{A^{i,i+1}} - \frac{K_1^i}{K_1} \right| \tag{3}$$

where the material parameters A and K_1 and the domain wall width δ_B refer to the matrix phase. From eq. (3) we derive the microstructural parameter

$$\alpha_{K,pin} = \frac{\pi}{3\sqrt{3}} \frac{d}{\delta_B} \left| \sum_{i=1}^{n-1} \frac{A}{A^{i,i+1}} - \frac{K_1^i}{K_1} \right| . \tag{4}$$

For a numerical evaluation of $\alpha_{K,pin}$ we assume $A^{i,i+1} \approx A$ because both phases have similar Curie temperatures. An approximate value of $\alpha_{K,pin}$ can be estimated under the assumption of

a linear increase of K_1^* from K_1 to $3K_1$ which extends over $n = 10$ layers. For the wall width $\delta_B = \pi(A^{2:17}/K_1^{*2:17})^{0.5}$ we receive with $A^{2:17} = 9.5\,10^{-12}$ J/m and $K_1^{*2:17} = 2.91$ MJ/m^3 $\delta_B = 5.7$ nm. From eq.(4) we then obtain $\alpha_{K,pin} = 0.35$ in agreement with the experimental value of $\approx$0.4. Accordingly, the two expressions for estimating the coercivity lead to a rather accessible explanation of the temperature coefficients of the coercivity. In general, the temperature stability of the coercive field is better for Cu-poor cell walls than for Cu-rich ones [6,16]. This is due to the fact that in the Cu-poor case the equilibrium of the decomposition reaction mentioned above is not completely shifted to the left so that the 1:5 phase is diluted by the remaining phases resulting in a reduction of its intrinsic magnetic parameters and therefore showing over a large temperature range a similar K_1 (and therefore γ) behaviour as the 2:17 cell phase (figure 14 (left)). The Cu content of the cell walls is influenced by both the Cu content of the sample itself and the cell size. Usually, if the cell size is small which can be realized by a low Fe content, a high Zr content and a smaller TM:RE ratio z ($z \leq 7.0$) the Cu content of the cell walls is also small. Similarly, magnets which have not been heat treated optimally (T_a too low, t_a too short) also show smaller cell sizes and therefore less Cu in the cell walls. In contrast, in the Cu-rich case the equilibrium is completely shifted to the left leading to a entirely different temperature behaviour of the wall energies $\gamma^{1:5}$ and $\gamma^{2:17}$ and therefore to a strongly negative temperature coefficient of the coercivity according to eq.(2) and eq.(3). In any case, at low temperatures the pinning is repulsive and changes to an attractive one at temperatures between 400 K and 700 K depending on the Cu content. The smaller the Cu content of the cell walls the higher the temperature of the cross-over and the Curie temperature of the 1:5 phase. Although the coercivity is determined by the difference in the domain wall energies, $\mu_0 H_C$ never becomes zero at the temperature of the cross-over. This is because $\Delta\gamma$ does not become equal zero everywhere in the cell walls at the same temperature due to local fluctuations of the 1:5 composition. Consequently, as the crossing angle β is larger for Cu-rich samples, $\mu_0 H_C(T)$ is not influenced by the cross-over. However, as in Cu-poor samples β is very small the crossing manifests in an anomalous (positive) temperature coefficient. As soon as the 1:5 phase reaches its Curie temperature (which is always smaller than that of the 2:17 phase) it seems to be possible that the pinning behaviour changes to a nucleation behaviour with the cells magnetically isolated by the paramagnetic 1:5 boundaries. This behaviour was observed by Tellez-Blanco et al. [31]. In figure 14 (right) the temperature dependence of the coercivity is presented for some fully heat treated melt-spun pms for which a very similar behaviour concerning microstructure and magnetic properties can be realized after applying an appropriate annealing procedure [32]. To illustrate impressively the suitability of 2:17 type Sm-Co based pms for high temperature applications the temperature behaviour is compared to three other common pm materials, namely $Nd_2Fe_{14}B$, a Sr ferrite and AlNiCo.

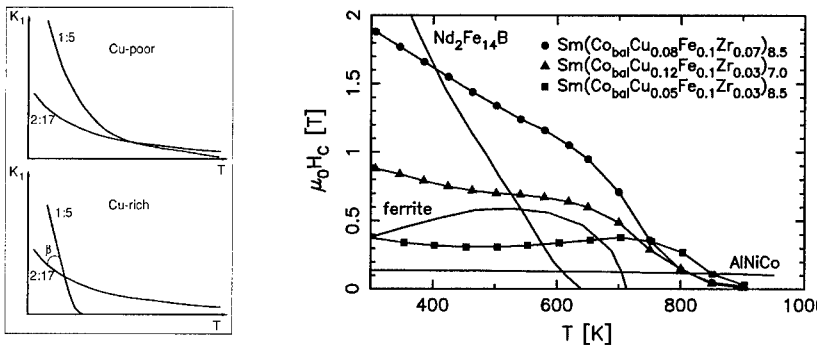

Figure 14. Temperature dependence of the magnetocrystalline anisotropy constant schematically (*left*) and of the coercivity of different fully heat treated melt-spun pms compared to other common pm materials (*right*).

ACKNOWLEDGEMENT

The authors wish to thank Dr. M. Grönefeld (Magnetfabrik Bonn, GmbH, Germany) for the industrial fabrication of their melt-spun ribbon material into bonded magnets and the company Electron Energy Corporation (EEC), Landisville, USA, for providing a solution-treated $Sm_2(Co,Cu,Fe,Zr)_{17}$ sintered magnet. Furthermore, they are grateful to Dr. C. Skokov for putting Figure 12 (right) at their disposal.

REFERENCES

[1] K.J. Strnat, G. Hoffer, J.C. Olsen, W. Ostertag, J.J. Becker, J. Appl. Phys. **38**, 1001 (1967).
[2] J.J. Croat, J.F. Herbst, R.W. Lee, F.E. Pinkerton, J. Appl. Phys. **55**, 2078 (1984).
[3] M. Sagawa, S. Fujimura, M. Togawa, Y. Matsuura, J. Appl. Phys. **55**, 2083 (1984).
[4] G.C. Hadjipanayis, R.C. Hazzleton, K.R. Lawless, J. Appl. Phys. **55**, 2073 (1984).
[5] K.H.J. Buschow, in *Handbook of Magnetic Materials*, ed. K.H.J. Buschow (Elsevier, North-Holland-Amsterdam), Vol. 10 (1997) 463.
[6] J.F. Liu, Y. Zhang, Y. Ding, D. Dimitrov, G.C. Hadjipanayis, in *Proceedings of the 15th International Workshop on REM and their applications*, Dresden, Germany, ed. L. Schultz, K.H. Müller (1998) 607.
[7] C.H. Chen, M.S. Walmer, M.H. Walmer, S. Liu, E. Kuhl, G. Simon, *J. Appl. Phys.* **83**, 6706 (1998).
[8] H. Kronmüller, in *Supermagnets, hard magnetic materials*, Kluwer, Dordrecht, eds. G.J. Long, F. Grandjean (1991) 461.
[9] A. Manaf, R.A. Buckley, H.A. Davies, M. Leonowicz: *J. Magn. Magn. Mater.* **101**, 360 (1991).
[10] J. Bauer, M. Seeger, A. Zern, H. Kronmüller: *J. Appl. Phys.* **80**, 1667 (1996).
[11] D. Goll, M. Seeger, H. Kronmüller: *J. Magn. Magn. Mater.* **185**, 49 (1998).
[12] E.F. Kneller, R. Hawig, *IEEE Trans. Magn.* **27**, 3588 (1991).
[13] A. Manaf, M.A. Al-Khafaji, P.Z. Zhang, H.A. Davies, R.A. Buckley, W.M. Rainforth, *J. Magn. Magn. Mater.* **128**, 307 (1993).
[14] W. Gong, G.C. Hadjipanayis, R.I. Krause, *J. Appl. Phys.* **75**, 6649 (1994).
[15] H. Kronmüller, R. Fischer, M. Bachmann, T. Leineweber, *J. Magn. Magn. Mater.* **203**, 12 (1999).
[16] D. Goll, H. Kronmüller, *Naturwissenschaften* **87**, 423 (2000).
[17] H. Kronmüller, R. Fischer, M. Seeger, A. Zern, *J. Phys. D* **29**, 2274 (1996).
[18] H. Kronmüller, in *Proc. 11th Int. Symp. Magnetic Anisotropy and Coercivity in Rare Earth – Transition Metal Alloys*, Sendai, Japan, eds. H. Kaneko et al. (2000) S83.
[19] C. Maury, L. Rabenberg, C.H. Allibert, *phys. stat. sol. (a)* **140**, 57 (1993).
[20] A.E. Ray, S. Liu, in *Proceedings of the 12th International Workshop on REM and Their Applications*, Canberra, 1992, p.552.
[21] M. Katter, J. Weber, W. Assmus, P. Schrey, W. Rodewald, *IEEE Trans. Magn.* **32**, 4815 (1996).
[22] International Centre for Diffraction Data, U.S.A.: Powder Diffraction File.
[23] Y. Khan, *Z. Metallkd.* **65**, 489 (1974).
[24] H.H. Stadelmeier, B. Reinsch, G. Petzow, *Z. Metallkd.* **89**, 2 (1998).
[25] A.J. Percy, *J. Less Common Met.* **51**, 153 (1977).
[26] E. Lectard, C.H. Allibert, R. Ballou, *J. Appl. Phys.* **75**, 6277 (1994).
[27] D. Goll, W. Sigle, G.C. Hadjipanayis, H. Kronmüller, in *Proc. 16th Int. Workshop on RE-Magnets and their Applications*, Sendai, Japan, eds. H. Kaneko et al. (2000) 61.
[28] H. Kronmüller, K.D. Durst, W. Ervens, F. Fernengel, *IEEE Trans. Magn.* **20**, 1569 (1984).
[29] H.R. Hilzinger, *Appl. Phys.* **12**, 253 (1977).
[30] H.R. Hilzinger, H. Kronmüller, *Phys. Letters* **51A**, 59 (1975).
[31] J.C. Tellez-Blanco, X.C. Kou, R. Grössinger, E. Estevez-Rams, J. Fidler, B.M. Ma, in *Proc. 14th Int. Workshop on RE-Magnets and their Applications*, World Scientific, Singapore, eds. F.P. Missell et al., 707 (1996).
[32] D. Goll, I. Kleinschroth, W. Sigle, H. Kronmüller, *Appl. Phys. Lett.* **76**, 1054 (2000).